Research Paper
Computational Methods for Differential Equations
http://cmde.tabrizu.ac.ir
Vol. *, No. *, *, pp. 1-26
DOI:10.22034/cmde.2026.67493.3219

Numerical simulation of Kelvin-Helmholtz instability using split-step Fourier and exponential time-integrators

Kolade M. Owolabi*
[1]Department of Mathematical Sciences, Federal University of Technology Akure, PMB 704, Akure, Ondo State, Nigeria.
[2]Department of Software Engineering, Faculty of Engineering and Natural Sciences, Fenerbahçe University, Istanbul 34758, Turkiye.
[3]Department of Mathematics and Applied Mathematics, School of Science and Technology, Sefako Makgatho Health Sciences University, Ga-Rankuwa 0208, South Africa.

Abstract

This paper presents a high-order numerical framework that combines the split-step Fourier method (SSFM) with the exponential time-differencing Runge–Kutta 4 (ETDRK4) scheme for the simulation of two-dimensional incompressible Navier–Stokes flows exhibiting Kelvin–Helmholtz instability (KHI). The proposed approach employs Fourier pseudo-spectral discretization to achieve spectral spatial accuracy, while the ETDRK4 integrator efficiently treats the stiff viscous diffusion operator, resulting in a robust and accurate solver for shear-layer evolution, vortex roll-up, and nonlinear instability development. The numerical method is validated against analytical linear growth rates of the Kelvin–Helmholtz instability and further assessed through comprehensive spatial and temporal convergence studies. A comparative study with the classical fourth-order Runge–Kutta (RK4) method demonstrates that the proposed SSFM–ETDRK4 framework consistently achieves smaller numerical errors while maintaining fourth-order temporal accuracy. The convergence results confirm exponential spatial accuracy and excellent numerical stability, enabling the accurate resolution of fine-scale vortical structures and long-time flow evolution. These findings establish the proposed SSFM–ETDRK4 framework as an efficient and reliable computational tool for simulating Kelvin–Helmholtz instability and related incompressible shear-flow problems encountered in geophysical, astrophysical, and engineering applications.

Keywords. Kelvin–Helmholtz instability, Split-step Fourier method, Vorticity, Hydrodynamic instabilities, Numerical simulations.
2010 Mathematics Subject Classification. 35Q35, 76M22, 76E17, 65M70.

1. Introduction

The Kelvin–Helmholtz instability (KHI) is a fundamental hydrodynamic phenomenon that occurs at the interface between two fluids with differing velocities. It is characterized by the growth of perturbations at the interface, leading to the development of vortical structures and, eventually, turbulent mixing. This instability plays a crucial role in various physical and engineering applications, including atmospheric dynamics, oceanography, astrophysical jets, and inertial confinement fusion [6, 9].

Over the past decades, numerous analytical and numerical studies have been conducted to investigate the nonlinear development of the KHI. Early theoretical works focused on linear stability analysis in idealized settings [3, 15, 17], which provided significant insights into growth rates and threshold conditions. However, the fully nonlinear evolution of the instability and the transition to turbulence require robust and accurate numerical simulations.

Traditional numerical approaches for simulating KHI include finite difference methods (FDM), finite volume methods (FVM), and finite element methods (FEM). These methods are widely used due to their flexibility in handling complex geometries and boundary conditions [14]. However, they often suffer from numerical dispersion and dissipation, particularly in the presence of small-scale structures and high Reynolds number flows. High-order methods such

Received: 24 May 2025; Accepted: 23 September 2026.
∗ Corresponding author. Email: mkowolax@yahoo.com, kmowolabi@futa.edu.ng.

as discontinuous Galerkin and spectral element methods have been introduced to improve resolution and accuracy [10, 13], but these come at increased computational costs.

Spectral methods, especially those based on Fourier transforms, offer an attractive alternative for problems with periodic boundary conditions and smooth solutions [4]. Spectral and pseudo-spectral methods have gained popularity due to their spectral convergence and high accuracy for smooth problems with periodic boundary conditions [4]. These methods transform differential operators into algebraic operations in Fourier space, significantly reducing computational cost while maintaining accuracy. The split-step Fourier method (SSFM) leverages this property by splitting the linear and nonlinear components of the governing equations and integrating them separately in Fourier and physical space, respectively. This approach has proven effective in nonlinear Schrödinger equations and fluid instabilities [21]. These methods exhibit exponential convergence for sufficiently smooth functions and allow for efficient implementation via the Fast Fourier Transform (FFT). In the context of KHI, spectral methods are particularly effective in resolving the fine-scale vorticity structures that emerge during the nonlinear stages of the instability [11].

Time integration presents another significant challenge, especially for stiff systems arising from viscous or diffusive terms. Explicit schemes are subject to severe time-step restrictions, while fully implicit schemes can be computationally expensive. Exponential time differencing (ETD) methods, such as the fourth-order ETDRK4 scheme introduced by Cox and Matthews [7], address this challenge by integrating the linear stiff part exactly and treating the nonlinear part with a Runge–Kutta method. This approach enables larger time steps while preserving stability and accuracy.

On the temporal side, the treatment of stiff diffusive terms in the Navier–Stokes equations remains a challenge. Traditional explicit schemes are constrained by severe time step restrictions due to stability conditions. Implicit schemes, while stable, are computationally expensive and can suffer from reduced accuracy. Exponential Time Differencing Runge–Kutta methods (ETDRK4), introduced by Cox and Matthews, offer an elegant solution by integrating the stiff linear terms exactly and applying Runge–Kutta methods to the nonlinear remainder. The ETDRK4 method, in particular, combines high-order accuracy with excellent stability properties, making it well-suited for simulating the evolution of vortical flows.

Despite the advancements in numerical modeling of KHI, there remain open questions related to the accurate long-time evolution of vortical structures, preservation of physical invariants (e.g., enstrophy), and the influence of small-scale features in highly resolved simulations. Many existing schemes trade off accuracy for stability or are not optimized for parallel computation. The combination of SSFM and ETDRK4 provides a compelling framework by combining the best of spatial and temporal discretizations.

The combination of Fourier spectral methods for spatial discretization with ETDRK4 for temporal integration thus forms a powerful framework for simulating the KHI in periodic domains. This paper contributes to the literature by developing a robust and high-accuracy solver that leverages this combination. Compared to previous works, our method provides enhanced resolution of vorticity dynamics and improved computational efficiency. Furthermore, we address the need for detailed mathematical formulation, implementation guidance, and a systematic analysis of stability and convergence—gaps that are often underrepresented in numerical KHI studies.

2. Formulation of KHI-like Family Models and Applications

Kelvin–Helmholtz instability (KHI) emerges in shear flows where a velocity discontinuity or gradient exists between two fluid layers. The underlying mechanism of KHI arises due to the vorticity generation and growth of interface perturbations, which lead to vortex roll-up and mixing phenomena. The KHI framework forms the basis of a broader class of shear-driven and interface instabilities, which are relevant across multiple domains including fluid dynamics, plasma physics, atmospheric science, chemi...

2.1. **Canonical form of KHI equations.**

The classical Kelvin–Helmholtz instability (KHI) arises in an incompressible, inviscid, two-dimensional fluid governed by the Euler equations. These equations describe the conservation of momentum and mass:

$$\begin{aligned} \frac{\partial \mathbf{u}}{\partial t} + (\mathbf{u}\cdot\nabla)\mathbf{u} &= -\nabla p, \\ \nabla\cdot\mathbf{u} &= 0, \end{aligned} \tag{2.1}$$

where $\mathbf{u} = (u, v)$ is the velocity field and p is the pressure. The first equation represents the momentum balance in the absence of viscosity, and the second enforces the incompressibility condition.

To investigate the onset of instability, we consider a base flow of the form $\mathbf{U} = (U(y), 0)$, where the horizontal velocity varies in the vertical direction and the vertical velocity is initially zero. A commonly used profile for shear flow is the hyperbolic tangent jet:

$$U(y) = U_0 \tanh\left(\frac{y}{\delta}\right), \tag{2.2}$$

where U_0 is the characteristic velocity and δ represents the shear layer thickness. This base flow models a smooth transition between two streams moving in opposite directions and is symmetric about $y = 0$.

We introduce small perturbations $\tilde{\mathbf{u}} = (u', v')$, $\tilde{p} = p'$, and linearize the Euler equations about the base flow:

$$\mathbf{u} = \mathbf{U}(y) + \tilde{\mathbf{u}}(x, y, t), \quad p = P(y) + \tilde{p}(x, y, t). \tag{2.3}$$

Assuming normal-mode perturbations of the form

$$\tilde{\mathbf{u}}(x, y, t), \tilde{p}(x, y, t) \propto e^{i(kx - \omega t)},$$

where k is the wave number and ω the complex frequency, the linearized equations reduce to the well-known Rayleigh equation for the streamfunction ψ, defined via $u' = \partial\psi/\partial y$, $v' = -\partial\psi/\partial x$:

$$(U(y) - c)\left(\frac{d^2\psi}{dy^2} - k^2\psi\right) - \frac{d^2U}{dy^2}\psi = 0, \tag{2.4}$$

where $c = \omega/k$ is the phase speed of the disturbance. Equation (2.4) is an eigenvalue problem that governs the stability of inviscid shear flows. The boundary conditions typically require $\psi \to 0$ as $|y| \to \infty$ for unbounded domains.

A complex value of ω with positive imaginary part $\Im(\omega) > 0$ indicates that the corresponding mode grows exponentially in time, signifying linear instability. For the hyperbolic tangent profile, it is well known that the flow is unstable to long-wavelength disturbances when δ is sufficiently small.

Physically, the instability originates from the inflection point in the velocity profile $U(y)$, which satisfies Rayleigh's inflection point theorem — a necessary condition for instability in inviscid parallel flows. In the nonlinear regime, the initially small perturbations evolve into rolling vortices, a phenomenon captured in full numerical simulations and observed in both geophysical and laboratory shear flows.

While the above formulation provides essential theoretical insight, it does not capture viscous effects, which are important in more realistic settings. For high but finite Reynolds numbers, the Navier–Stokes equations are used, and viscosity introduces vorticity diffusion, vortex stretching, and possible transition to turbulence. In this work, we solve the incompressible Navier–Stokes equations numerically to capture the nonlinear development and saturation of the KHI.

2.2. **KHI with viscosity and diffusion.** To incorporate the effects of molecular viscosity and scalar diffusion, the dynamics of the Kelvin–Helmholtz instability (KHI) are governed by the incompressible Navier–Stokes equations:

$$\begin{aligned} \frac{\partial \mathbf{u}}{\partial t} + (\mathbf{u} \cdot \nabla)\mathbf{u} &= -\nabla p + \nu \nabla^2 \mathbf{u}, \\ \nabla \cdot \mathbf{u} &= 0, \end{aligned} \tag{2.5}$$

where $\mathbf{u} = (u, v)$ is the velocity field, p is the pressure, and ν is the kinematic viscosity. These equations extend the ideal (Euler) fluid model by accounting for internal friction and diffusion of momentum, which become significant at finite Reynolds numbers.

The viscosity term $\nu\nabla^2\mathbf{u}$ plays a crucial role in the evolution of the shear layer and the subsequent formation of coherent vortical structures. In contrast to the inviscid case, where small-scale perturbations can grow without bound, viscosity introduces a damping mechanism that regularizes the flow and prevents the formation of unphysical singularities.

At moderate to high Reynolds numbers, the flow remains susceptible to the Kelvin–Helmholtz instability, but the growth rate and morphology of the instability are modified by viscous effects. The instability manifests as the roll-up of the shear layer into elliptical vortex structures, which may further interact, merge, or break down into smaller

vortices, depending on the flow regime. This transition from linear to nonlinear dynamics is strongly influenced by both the viscosity ν and the nature of the initial perturbations.

In many physical systems, KHI occurs in the presence of additional transported scalar fields such as temperature, concentration, or density. These are governed by advection-diffusion equations of the form:

$$\frac{\partial \phi}{\partial t} + (\mathbf{u} \cdot \nabla)\phi = D\nabla^2 \phi, \tag{2.6}$$

where ϕ represents a generic scalar field and D is the molecular diffusivity. For example, in stratified fluids, ϕ could represent density variations that interact with the velocity field through buoyancy effects, introducing baroclinic torque that alters the vorticity dynamics. In such cases, the interplay between velocity and scalar gradients can either stabilize or destabilize the flow, leading to phenomena such as double-diffusive instabilities or density-driven suppression of vortex growth.

Furthermore, the presence of viscosity introduces vorticity diffusion, which smoothens sharp gradients and leads to the eventual dissipation of kinetic energy. The evolution of the vorticity field $\omega = \nabla \times \mathbf{u}$ can be expressed in two dimensions as:

$$\frac{\partial \omega}{\partial t} + (\mathbf{u} \cdot \nabla)\omega = \nu\nabla^2 \omega, \tag{2.7}$$

which is particularly advantageous for spectral and pseudo-spectral numerical methods, as it eliminates the pressure term by combining the momentum and continuity equations into a single scalar equation.

In summary, the inclusion of viscosity and scalar diffusion significantly enriches the dynamical behavior of the KHI, allowing for a more realistic representation of mixing, turbulence transition, and energy dissipation. Numerical simulations based on the Navier–Stokes formulation provide detailed insights into these processes and are essential for capturing the full spectrum of KHI dynamics in both laboratory and geophysical contexts.

2.3. **Vortex sheet and vorticity-based formulation.** An alternative and widely used approach to modeling two-dimensional incompressible flows, particularly relevant in the context of shear-driven instabilities like the Kelvin–Helmholtz instability (KHI), is the vorticity–stream function formulation. This framework is especially advantageous for numerical simulations as it eliminates the pressure term and automatically enforces the incompressibility condition.

The governing equations in this formulation are:

$$\begin{aligned} \frac{\partial \omega}{\partial t} + \mathbf{u} \cdot \nabla\omega &= \nu\nabla^2 \omega, \\ \nabla^2 \psi &= -\omega, \\ \mathbf{u} &= \nabla^{\perp}\psi = (-\partial_y \psi, \partial_x \psi), \end{aligned} \tag{2.8}$$

where $\omega = \partial_x v - \partial_y u$ is the scalar vorticity, ψ is the stream function, and the velocity field $\mathbf{u} = (u, v)$ is recovered from ψ using the orthogonal gradient operator $\nabla^{\perp}$.

This formulation is particularly well-suited for analyzing vortex dynamics and the evolution of coherent structures. In the inviscid limit ($\nu = 0$), the vorticity is conserved along particle paths, i.e., it is materially advected. However, in the presence of viscosity, vorticity undergoes diffusion, which influences vortex stretching, reconnection, and eventual dissipation.

In the case of KHI, the initial condition often consists of a sharp velocity discontinuity across a shear layer, leading to a piecewise constant vorticity field, this is commonly referred to as a vortex sheet. Mathematically, a vortex sheet is a hypersurface across which the tangential component of the velocity has a jump discontinuity, while the normal component is continuous. These discontinuities can be modeled as singular distributions of vorticity, typically represented using Dirac delta functions in theoretical analyses. In practical simulations, however, the vortex sheet is regularized, and a smooth profile (e.g., hyperbolic tangent) is used to approximate the shear layer.

The dynamics of the vortex sheet under the KHI mechanism lead to the roll-up of the sheet into a train of counter-rotating vortices. This roll-up is captured with high fidelity in the vorticity formulation, as it tracks the evolution of rotational motion directly, bypassing the need to compute pressure. The numerical advantage is twofold: first, it

reduces the system from a vectorial PDE (Navier–Stokes) to a scalar PDE for ω; second, it simplifies the imposition of incompressibility.

The Biot–Savart law, implicit in the velocity recovery step $\mathbf{u} = \nabla^{\perp}\psi$, guarantees that the velocity field derived from the vorticity is divergence-free. The coupling between the vorticity and the stream function through the Poisson equation $\nabla^2\psi = -\omega$ forms the backbone of spectral and pseudo-spectral methods commonly used in computational fluid dynamics (CFD).

Moreover, this formulation lends itself well to spectral accuracy in periodic domains, enabling precise resolution of fine-scale vortex structures with minimal numerical diffusion. The method is also highly compatible with vortex methods, which discretize vorticity using Lagrangian particles and have been successfully applied to simulate vortex sheet dynamics with high accuracy.

In summary, the vorticity–stream function formulation provides both analytical clarity and computational efficiency in studying KHI and related shear flow instabilities. It is instrumental in capturing the evolution, roll-up, and merging of vortices and serves as a foundational framework for both theoretical investigations and high-resolution numerical simulations of two-dimensional incompressible flows.

2.4. **Potential Extension to Magnetohydrodynamic Flows.** The numerical framework developed in this work can be extended to magnetohydrodynamic (MHD) models describing electrically conducting fluids such as plasmas, liquid metals, and astrophysical flows. In such cases, the incompressible Navier–Stokes equations are coupled with the magnetic induction equation, yielding the ideal MHD system

$$\begin{aligned} \frac{\partial \rho}{\partial t} + \nabla \cdot (\rho \mathbf{u}) &= 0, \\ \frac{\partial (\rho \mathbf{u})}{\partial t} + \nabla \cdot (\rho \mathbf{u} \otimes \mathbf{u} + p\mathbb{I} - \mathbf{B} \otimes \mathbf{B}) &= 0, \\ \frac{\partial \mathbf{B}}{\partial t} - \nabla \times (\mathbf{u} \times \mathbf{B}) &= 0, \\ \nabla \cdot \mathbf{B} &= 0, \end{aligned} \tag{2.9}$$

where ρ, $\mathbf{u}$, p, and $\mathbf{B}$ denote the density, velocity, pressure, and magnetic field, respectively.

The presence of the magnetic field modifies the classical Kelvin–Helmholtz instability through magnetic pressure and magnetic tension, which can either suppress or alter the growth of unstable shear modes depending on the field orientation and strength. Consequently, MHD Kelvin–Helmholtz instability plays an important role in plasma transport, solar wind interactions, magnetospheric dynamics, and astrophysical jet evolution.

Although the proposed SSFM–ETDRK4 methodology can be naturally extended to the MHD equations by incorporating the magnetic induction equation into the Fourier pseudo-spectral framework, such an extension is beyond the scope of the present study. Throughout this paper, all numerical experiments are performed exclusively for the classical incompressible Navier–Stokes formulation of the Kelvin–Helmholtz instability. The MHD model is included only to illustrate the broader applicability of the proposed numerical methodology.

2.5. **Potential Extension to Diffuse-Interface Models.** The proposed SSFM–ETDRK4 framework can be naturally extended to diffuse-interface models for multiphase flows, where interfaces are represented by a continuous phase-field variable rather than explicit interface tracking. Among the most widely used formulations is the coupled Navier–Stokes–Cahn–Hilliard (NSCH) system, which provides a thermodynamically consistent description of two-phase incompressible flows. A general form of the governing equations is given by

$$\begin{aligned} \frac{\partial \phi}{\partial t} + \mathbf{u} \cdot \nabla \phi &= M \nabla^2 \mu, \\ \mu &= \frac{\delta \mathcal{F}}{\delta \phi}, \\ \frac{\partial \mathbf{u}}{\partial t} + \mathbf{u} \cdot \nabla \mathbf{u} &= -\nabla p + \nu \nabla^2 \mathbf{u} + \phi \nabla \mu, \\ \nabla \cdot \mathbf{u} &= 0, \end{aligned} \tag{2.10}$$

where ϕ denotes the phase-field variable, μ is the chemical potential derived from the free-energy functional $\mathcal{F}$, and M is the mobility coefficient. The additional capillary force $\phi\nabla\mu$ accounts for interfacial effects and enables the simulation of complex interface deformation, coalescence, and breakup.

From a numerical perspective, the SSFM–ETDRK4 methodology developed in this work is readily applicable to the NSCH system. The linear diffusion operators in both the momentum and phase-field equations can be treated using exponential time differencing, while the nonlinear convective and coupling terms are evaluated within the same Fourier pseudo-spectral framework. Consequently, the proposed solver provides a flexible computational foundation for diffuse-interface multiphase flow simulations.

It should be emphasized, however, that the Navier–Stokes–Cahn–Hilliard model is *not* employed in the numerical experiments presented in this paper. All validation studies and Kelvin–Helmholtz instability simulations reported in Sections 4 and 5 are performed exclusively for the classical incompressible Navier–Stokes formulation. The NSCH model is included only to illustrate a potential extension of the proposed SSFM–ETDRK4 methodology to more general multiphase flow problems and is left for future investigation.

2.6. **Representative Applications of Kelvin–Helmholtz Instability.** The Kelvin–Helmholtz instability is a fundamental mechanism responsible for mixing, momentum transfer, and vortex formation in shear-driven flows. Owing to its universal nature, it arises in a wide range of scientific and engineering applications. In atmospheric and oceanic flows, KHI contributes to the formation of wave clouds, stratified mixing, and the evolution of jet streams and thermoclines [19]. In astrophysical and space plasmas, it governs shear-layer dynamics in accretion disks, stellar winds, astrophysical jets, and planetary magnetospheres, where it promotes turbulence and energy transport [1, 16]. Engineering applications include high-speed shear layers, turbulent mixing, combustion systems, jet propulsion, and fluid machinery, where accurate prediction of instability growth is essential for improving efficiency and performance [8]. At smaller scales, Kelvin–Helmholtz instability also enhances interfacial mixing in microfluidic devices and multiphase transport processes [18].

The broad occurrence of Kelvin–Helmholtz instability across these diverse physical systems highlights the need for accurate and computationally efficient numerical methods capable of resolving both the linear growth and nonlinear evolution of shear instabilities. This work focuses specifically on the development and validation of an SSFM–ETDRK4 framework for the classical incompressible Kelvin–Helmholtz problem, while the broader application areas discussed above provide motivation for the wider applicability of the proposed numerical methodology.

3. Theoretical Results on the KHI-like Models

This section provides rigorous theoretical results regarding the well-posedness, energy conservation, and linear stability of Kelvin–Helmholtz-type models under simplifying assumptions. These foundational theorems ensure the legitimacy of numerical schemes applied in later sections.

3.1. **Existence and uniqueness of solutions.** We recall the incompressible Euler system on $\mathbb{R}^2$,

$$\begin{cases} \partial_t \mathbf{u} + (\mathbf{u}\cdot\nabla)\mathbf{u} + \nabla p = 0, \\ \nabla\cdot\mathbf{u} = 0, \qquad\qquad (x,t)\in\mathbb{R}^2\times[0,\infty), \\ \mathbf{u}|_{t=0} = \mathbf{u}_0, \end{cases} \tag{3.1}$$

and prove the classical local well-posedness in H^s for $s > 2$.

Theorem 3.1 (Local Well-posedness)**.** *Let $\mathbf{u}_0 \in H^s(\mathbb{R}^2)$ be divergence-free with $s > 2$. Then there exists $T = T(\|\mathbf{u}_0\|_{H^s}) > 0$ and a unique solution*

$$\mathbf{u} \in C([0,T]; H^s(\mathbb{R}^2)) \cap C^1([0,T]; H^{s-1}(\mathbb{R}^2)),$$

solving (2.1) in the sense of distributions. Moreover, $\|\mathbf{u}(t)\|_{H^s}$ depends continuously on t and on the data.

Proof. The proof relies on a Picard iteration for a sequence of linear transport systems together with commutator estimates in H^s. Since $\nabla \cdot \mathbf{u} = 0$, we may eliminate the pressure either by applying the Leray projector $\mathbb{P}$ onto divergence-free vector fields (bounded on H^s), which yields the projected form

$$\partial_t \mathbf{u} + \mathbb{P}(\mathbf{u} \cdot \nabla \mathbf{u}) = 0, \qquad \mathbf{u}|_{t=0} = \mathbf{u}_0,$$

or keep p and note that it plays no role in the basic H^s energy estimate because $\langle \Lambda^s \nabla p, \Lambda^s \mathbf{u} \rangle_{L^2} = 0$ by incompressibility and integration by parts. Here $\Lambda^s = (I - \Delta)^{s/2}$ denotes the standard Bessel potential.

Fix $s > 2$. By Sobolev embedding in two dimensions, $H^s(\mathbb{R}^2) \hookrightarrow C^{1,\alpha}(\mathbb{R}^2)$ for some $\alpha = s - 2 > 0$, so in particular $\|\nabla \mathbf{v}\|_{L^\infty} \lesssim \|\mathbf{v}\|_{H^s}$ for any $\mathbf{v} \in H^s$. Define $\mathbf{u}^{(0)} := \mathbf{u}_0$ and, for $n \geq 0$, let $\mathbf{u}^{(n+1)}$ solve the linear, divergence-free transport system

$$\begin{cases} \partial_t \mathbf{u}^{(n+1)} + (\mathbf{u}^{(n)} \cdot \nabla)\mathbf{u}^{(n+1)} + \nabla p^{(n+1)} = 0, \\ \nabla \cdot \mathbf{u}^{(n+1)} = 0, \\ \mathbf{u}^{(n+1)}|_{t=0} = \mathbf{u}_0. \end{cases} \tag{3.2}$$

For each n, the coefficient field $\mathbf{u}^{(n)}$ is Lipschitz on any interval where it remains in H^s, hence (3.2) has a unique solution $\mathbf{u}^{(n+1)} \in C([0, T_n]; H^s)$ obtained by the method of characteristics or standard theory for linear transport with Lipschitz velocity, and T_n depends only on $\sup_{t \in [0,T_n]} \|\nabla \mathbf{u}^{(n)}(t)\|_{L^\infty}$.

We derive an H^s a priori bound uniform in n on a short interval. Applying Λ^s to the first equation in (3.2), taking the L^2 inner product with $\Lambda^s \mathbf{u}^{(n+1)}$, and using that $\nabla \cdot \mathbf{u}^{(n)} = 0$ gives

$$\frac{1}{2} \frac{d}{dt} \|\mathbf{u}^{(n+1)}\|_{H^s}^2 = -\big\langle \Lambda^s \big((\mathbf{u}^{(n)} \cdot \nabla)\mathbf{u}^{(n+1)} \big), \Lambda^s \mathbf{u}^{(n+1)} \big\rangle.$$

Decompose the nonlinear term via the commutator:

$$\Lambda^s \big((\mathbf{u}^{(n)} \cdot \nabla)\mathbf{u}^{(n+1)} \big) = (\mathbf{u}^{(n)} \cdot \nabla)\Lambda^s \mathbf{u}^{(n+1)} + \big[\Lambda^s, \mathbf{u}^{(n)} \cdot \nabla \big] \mathbf{u}^{(n+1)}.$$

The first term cancels after integrating by parts because $\nabla \cdot \mathbf{u}^{(n)} = 0$:

$$\big\langle (\mathbf{u}^{(n)} \cdot \nabla)\Lambda^s \mathbf{u}^{(n+1)}, \Lambda^s \mathbf{u}^{(n+1)} \big\rangle = \frac{1}{2} \int_{\mathbb{R}^2} (\nabla \cdot \mathbf{u}^{(n)}) \, |\Lambda^s \mathbf{u}^{(n+1)}|^2 \, dx = 0.$$

For the commutator we invoke a standard Kato–Ponce/Moser-type bound: for $s > 0$,

$$\big\| [\Lambda^s, \mathbf{v} \cdot \nabla] w \big\|_{L^2} \lesssim \|\nabla \mathbf{v}\|_{L^\infty} \|w\|_{H^{s-1}} + \|\mathbf{v}\|_{H^s} \|\nabla w\|_{L^\infty}.$$

With $w = \mathbf{u}^{(n+1)}$ and $\mathbf{v} = \mathbf{u}^{(n)}$, and using $s > 2$ to bound $H^s \hookrightarrow W^{1,\infty}$, we obtain

$$\Big| \big\langle [\Lambda^s, \mathbf{u}^{(n)} \cdot \nabla]\mathbf{u}^{(n+1)}, \Lambda^s \mathbf{u}^{(n+1)} \big\rangle \Big| \lesssim \|\nabla \mathbf{u}^{(n)}\|_{L^\infty} \|\mathbf{u}^{(n+1)}\|_{H^s}^2.$$

Therefore,

$$\frac{d}{dt} \|\mathbf{u}^{(n+1)}\|_{H^s}^2 \lesssim \|\nabla \mathbf{u}^{(n)}\|_{L^\infty} \|\mathbf{u}^{(n+1)}\|_{H^s}^2 \lesssim \|\mathbf{u}^{(n)}\|_{H^s} \|\mathbf{u}^{(n+1)}\|_{H^s}^2. \tag{3.3}$$

Set $M := 2\|\mathbf{u}_0\|_{H^s}$ and choose $T > 0$ so small that $\int_0^T \|\mathbf{u}^{(n)}(t)\|_{H^s} \, dt \leq c\,T\,M \leq \log 2$ with the implicit constant c from (3.3). Grönwall's inequality then yields the uniform bound $\sup_{t \in [0,T]} \|\mathbf{u}^{(n+1)}(t)\|_{H^s} \leq M$ provided $\sup_{t \in [0,T]} \|\mathbf{u}^{(n)}(t)\|_{H^s} \leq M$. Since this holds for $n = 0$ by definition, induction gives

$$\sup_{n \geq 0} \sup_{t \in [0,T]} \|\mathbf{u}^{(n)}(t)\|_{H^s} \leq M. \tag{3.4}$$

To establish convergence, consider the difference $\mathbf{w}^{(n+1)} := \mathbf{u}^{(n+1)} - \mathbf{u}^{(n)}$, which solves

$$\partial_t \mathbf{w}^{(n+1)} + (\mathbf{u}^{(n)} \cdot \nabla)\mathbf{w}^{(n+1)} + (\mathbf{w}^{(n)} \cdot \nabla)\mathbf{u}^{(n)} + \nabla q^{(n+1)} = 0, \qquad \nabla \cdot \mathbf{w}^{(n+1)} = 0, \qquad \mathbf{w}^{(n+1)}|_{t=0} = 0.$$

Taking the H^{s-1} inner product with $\mathbf{w}^{(n+1)}$ and repeating the commutator argument (now one derivative lower) gives

$$\frac{d}{dt} \|\mathbf{w}^{(n+1)}\|_{H^{s-1}}^2 \lesssim \|\nabla \mathbf{u}^{(n)}\|_{L^\infty} \|\mathbf{w}^{(n+1)}\|_{H^{s-1}}^2 + \|\nabla \mathbf{u}^{(n)}\|_{L^\infty} \|\mathbf{w}^{(n)}\|_{H^{s-1}} \|\mathbf{w}^{(n+1)}\|_{H^{s-1}}.$$

Using Young's inequality and the uniform bound (3.4), we arrive at

$$\frac{d}{dt}\|\mathbf{w}^{(n+1)}\|_{H^{s-1}} \;\le\; CM\,\|\mathbf{w}^{(n+1)}\|_{H^{s-1}} \;+\; CM\,\|\mathbf{w}^{(n)}\|_{H^{s-1}}.$$

By Grönwall and the choice of T (so that $CMT \le \frac{1}{2}$ after adjusting constants), this yields the contraction estimate

$$\sup_{t\in[0,T]}\|\mathbf{w}^{(n+1)}(t)\|_{H^{s-1}} \;\le\; \tfrac{1}{2}\sup_{t\in[0,T]}\|\mathbf{w}^{(n)}(t)\|_{H^{s-1}}.$$

Hence $(\mathbf{u}^{(n)})_{n\ge 0}$ is Cauchy in $C([0,T];H^{s-1})$, and by (3.4) it is bounded in $L^\infty([0,T];H^s)$. Interpolating in Sobolev spaces and using completeness, there exists $\mathbf{u}\in C([0,T];H^{s-1})\cap L^\infty([0,T];H^s)$ such that $\mathbf{u}^{(n)}\to\mathbf{u}$ in $C([0,T];H^{s-1})$ and weak-$*$ in $L^\infty([0,T];H^s)$. Passing to the limit in (3.2) yields that $\mathbf{u}$ solves (3.1) in distributions; the pressure p is recovered at each time by solving $-\Delta p = \partial_i\partial_j(u_iu_j)$, which is consistent since $u\in H^s$ with $s>2$ implies $u\otimes u\in H^s$ and hence $p\in H^{s+1}$ up to an additive function of time.

The energy inequality (3.3) with $\mathbf{u}^{(n)}$ replaced by $\mathbf{u}$ is stable under the above limit and gives

$$\frac{d}{dt}\|\mathbf{u}(t)\|_{H^s}^2 \;\lesssim\; \|\nabla\mathbf{u}(t)\|_{L^\infty}\,\|\mathbf{u}(t)\|_{H^s}^2 \;\lesssim\; \|\mathbf{u}(t)\|_{H^s}^3,$$

which ensures $\mathbf{u}\in C([0,T];H^s)$ by a standard ODE-in-Banach-space argument and the dominated convergence theorem, and shows the lifespan T can be chosen depending only on $\|\mathbf{u}_0\|_{H^s}$.

Uniqueness follows from a similar difference estimate at the H^{s-1} level. If $\mathbf{u},\mathbf{v}\in C([0,T];H^s)$ are two solutions with the same initial data, their difference $\mathbf{w}:=\mathbf{u}-\mathbf{v}$ obeys

$$\partial_t\mathbf{w} + (\mathbf{u}\cdot\nabla)\mathbf{w} + (\mathbf{w}\cdot\nabla)\mathbf{v} + \nabla q = 0, \qquad \nabla\cdot\mathbf{w} = 0, \qquad \mathbf{w}|_{t=0} = 0.$$

Taking the H^{s-1} inner product with $\mathbf{w}$ and using $H^s\hookrightarrow W^{1,\infty}$ gives

$$\frac{d}{dt}\|\mathbf{w}\|_{H^{s-1}} \;\le\; C\big(\|\nabla\mathbf{u}\|_{L^\infty} + \|\nabla\mathbf{v}\|_{L^\infty}\big)\,\|\mathbf{w}\|_{H^{s-1}}.$$

Grönwall and $\mathbf{w}(0)=0$ imply $\mathbf{w}\equiv 0$ on $[0,T]$. Continuous dependence on initial data is proved by the same estimate with nonzero initial difference. This completes the proof. □

3.2. **Conservation of kinetic energy.**

Theorem 3.2 (Energy conservation)**.** *Let $\mathbf{u}$ be a smooth solution to the incompressible Euler equations (2.1) on $\mathbb{R}^2$ (or on the 2-torus $\mathbb{T}^2$), and assume either sufficient spatial decay at infinity (for $\mathbb{R}^2$) or periodic boundary conditions (for $\mathbb{T}^2$) so that all integrations by parts below are justified. Then the kinetic energy*

$$E(t) = \frac{1}{2}\int_{\mathbb{R}^2}|\mathbf{u}(x,t)|^2\,dx$$

is conserved in time: $E(t)=E(0)$ for all t in the interval of existence.

Proof. Differentiate $E(t)$ with respect to time and use that $\mathbf{u}$ is smooth to pass the time derivative under the integral sign:

$$\frac{dE}{dt} = \frac{d}{dt}\left(\frac{1}{2}\int|\mathbf{u}|^2\,dx\right) = \int\mathbf{u}\cdot\partial_t\mathbf{u}\,dx.$$

Substitute the momentum equation $\partial_t\mathbf{u} = -(\mathbf{u}\cdot\nabla)\mathbf{u} - \nabla p$ to obtain

$$\frac{dE}{dt} = -\int\mathbf{u}\cdot(\mathbf{u}\cdot\nabla)\mathbf{u}\,dx - \int\mathbf{u}\cdot\nabla p\,dx.$$

Handle the convective term first. Using index notation (u_j denotes the j-th component, summation over repeated indices) we have

$$\mathbf{u}\cdot(\mathbf{u}\cdot\nabla)\mathbf{u} = u_ju_k\partial_ku_j.$$

Observe the identity

$$u_ju_k\partial_ku_j = \tfrac{1}{2}u_k\partial_k(u_ju_j) = \tfrac{1}{2}\partial_k\big(u_k|\mathbf{u}|^2\big) - \tfrac{1}{2}(\partial_ku_k)\,|\mathbf{u}|^2.$$

Because $\nabla \cdot \mathbf{u} = \partial_k u_k = 0$ by incompressibility, this simplifies to

$$\mathbf{u} \cdot (\mathbf{u} \cdot \nabla)\mathbf{u} = \tfrac{1}{2}\partial_k\big(u_k|\mathbf{u}|^2\big).$$

Integrating over the domain and using either decay at infinity (so the boundary integral vanishes) or periodicity yields

$$\int \mathbf{u} \cdot (\mathbf{u} \cdot \nabla)\mathbf{u}\, dx = \tfrac{1}{2}\int \partial_k\big(u_k|\mathbf{u}|^2\big)\, dx = 0.$$

Next treat the pressure term. Integrate by parts:

$$\int \mathbf{u} \cdot \nabla p\, dx = \int u_k \partial_k p\, dx = \int \partial_k(p u_k)\, dx - \int p\, \partial_k u_k\, dx.$$

Again incompressibility gives $\partial_k u_k = 0$, and the divergence term integrates to zero under the decay or periodicity hypotheses. Hence

$$\int \mathbf{u} \cdot \nabla p\, dx = 0.$$

Combining the two vanishing contributions yields $\dfrac{dE}{dt} = 0$. Therefore $E(t) = E(0)$ for all times in the interval of existence, completing the proof. □

3.3. **Linear instability criterion for shear layer.**

Theorem 3.3 (Rayleigh's inflection point criterion)**.** *Let $U(y)$ be a twice continuously differentiable shear profile on a domain $I \subset \mathbb{R}$ (either a finite channel $I = [a, b]$ with impermeable boundaries or the whole line with sufficient decay). Consider normal-mode perturbations of the form*

$$\psi(x, y, t) = \Re\{\phi(y)e^{i(kx-\omega t)}\},$$

with real wavenumber $k \neq 0$ and complex frequency $\omega = kc$. If the linearized inviscid (Euler) problem about $U(y)$ admits an exponentially growing mode (i.e. $\Im c > 0$), then $U''(y)$ must vanish at some point of I; in other words, a necessary condition for spectral instability is that U possess an inflection point.

Proof. Linearizing the two-dimensional incompressible Euler equations about the steady shear $U(y)\mathbf{e}_x$ and inserting the normal-mode ansatz leads to the Rayleigh eigenvalue problem for $\phi(y)$:

$$(U(y) - c)\big(\phi''(y) - k^2\phi(y)\big) - U''(y)\phi(y) = 0, \qquad y \in I, \tag{3.5}$$

together with boundary conditions $\phi(a) = \phi(b) = 0$ in the channel case, or the requirement that ϕ and its derivatives decay sufficiently fast as $|y| \to \infty$ on the whole line. We assume $\phi \not\equiv 0$ is an eigenfunction associated with a complex phase speed $c \in \mathbb{C}$; instability corresponds to $\Im c > 0$.

Multiply (3.5) by the complex conjugate $\overline{\phi}$ and divide by $U - c$ to obtain the identity (valid pointwise except at points where $U - c = 0$, which will be addressed by continuity arguments below)

$$\overline{\phi}\big(\phi'' - k^2\phi\big) - \frac{U''}{U - c}|\phi|^2 = 0.$$

Integrate over I and integrate the first term by parts. Using the boundary conditions (vanishing boundary term for the channel case, or decay at infinity for the whole-line case) we get

$$\int_I \overline{\phi}\phi''\, dy = -\int_I |\phi'|^2\, dy,$$

so that

$$-\int_I |\phi'|^2\, dy - k^2\int_I |\phi|^2\, dy - \int_I \frac{U''(y)}{U(y) - c}\,|\phi(y)|^2\, dy = 0, \tag{3.6}$$

or equivalently

$$\int_I \frac{U''(y)}{U(y) - c}\,|\phi(y)|^2\, dy = -\int_I \big(|\phi'|^2 + k^2|\phi|^2\big)\, dy.$$

The right-hand side is strictly negative because $\phi \not\equiv 0$ and $k \neq 0$. Separate the real and imaginary parts of the left-hand side. Write $c = c_r + ic_i$ with $c_i = \Im c$. For each y we have

$$\frac{1}{U(y)-c} = \frac{U(y)-c_r}{|U(y)-c|^2} + i\frac{c_i}{|U(y)-c|^2}.$$

Taking the imaginary part of the integrated identity (3.6) yields

$$\int_I \frac{U''(y)\, c_i}{|U(y)-c|^2}\,|\phi(y)|^2\,dy \;=\; 0.$$

If there is an unstable mode then $c_i > 0$, so we may divide by c_i to obtain

$$\int_I \frac{U''(y)}{|U(y)-c|^2}\,|\phi(y)|^2\,dy = 0. \tag{3.7}$$

The integrand in (3.7) is continuous except possibly at points where $U(y) = c_r$; however, since $|U-c|^2 = (U-c_r)^2 + c_i^2 \geq c_i^2 > 0$, no singularity occurs and the integrand is everywhere finite and continuous. Because $|\phi|^2/|U-c|^2$ is nonnegative and not identically zero (otherwise (3.6) would be impossible), the integral in (3.7) can vanish only if $U''(y)$ changes sign somewhere in I. In particular, U'' cannot be of one sign on the whole domain; hence there must exist at least one point $y_0 \in I$ where $U''(y_0) = 0$. This shows that a necessary condition for spectral instability ($\Im c > 0$) is that U have an inflection point.

A few remarks about the formal steps above: the division by $U - c$ is justified because for unstable modes $c_i \neq 0$ so $U(y) - c \neq 0$ for all real y. If one instead considers neutral modes with $c_i = 0$ the argument must be modified to treat critical layers where $U = c_r$; the statement of Rayleigh's criterion concerns unstable modes and is cleanest in the $c_i \neq 0$ case treated here. The boundary terms vanish under the stated boundary or decay hypotheses, completing the proof. □

3.4. **Maximum principle for the vorticity equation.** We consider the two-dimensional vorticity equation in viscous form

$$\partial_t \omega + \mathbf{u}\cdot\nabla\omega = \nu\Delta\omega, \tag{3.8}$$

where $\omega = \omega(x,t)$ is the scalar vorticity, $\mathbf{u} = \mathbf{u}(x,t)$ is a given velocity field satisfying $\nabla\cdot\mathbf{u} = 0$, and $\nu \geq 0$ is the kinematic viscosity. In the statements and proofs below we assume sufficient smoothness (classical solution) and either a bounded spatial domain $\Omega \subset \mathbb{R}^2$ with appropriate boundary conditions (e.g. no-slip or impermeable so that boundary terms are controlled) or the whole plane with sufficient decay at infinity so that integrations by parts are justified.

Theorem 3.4 (Vorticity maximum principle)**.** *Let $\omega \in C^{2,1}(\Omega\times[0,T])$ solve (3.8) with initial data $\omega_0 \in L^\infty(\Omega)$. If $\nu \geq 0$ and $\mathbf{u}$ is divergence free, then for all $t \in [0,T]$*

$$\|\omega(\cdot,t)\|_{L^\infty(\Omega)} \leq \|\omega_0\|_{L^\infty(\Omega)}.$$

In particular, when $\nu > 0$ the L^∞ norm is nonincreasing in time; when $\nu = 0$ (pure transport) the L^∞ norm is exactly preserved along characteristics.

Proof. We present two complementary arguments: a pointwise maximum principle argument (classical) and a L^p-argument that yields the same conclusion in a slightly different guise.

Pointwise maximum principle. Let $M := \|\omega_0\|_{L^\infty(\Omega)}$ and set $\varphi(x,t) := \omega(x,t) - M$. Then $\varphi(\cdot,0) \leq 0$ a.e. and φ satisfies

$$\partial_t\varphi + \mathbf{u}\cdot\nabla\varphi = \nu\Delta\varphi.$$

Suppose for contradiction that there exists a first time $t_* > 0$ and a point $x_* \in \Omega$ with $\varphi(x_*,t_*) > 0$. By continuity there is a first time $t_* > 0$ such that $\sup_{x\in\Omega}\varphi(\cdot,t_*) =: \delta > 0$ and this supremum is attained at some point $x_* \in \overline{\Omega}$. If x_* lies on the boundary then the boundary condition (or decay at infinity in the unbounded case) prevents a positive

maximum to appear there before it appears in the interior; hence we may assume x_* is an interior point. At the interior spatial maximum we have $\nabla\varphi(x_*,t_*)=0$ and $\Delta\varphi(x_*,t_*)\le 0$. Evaluating the PDE at (x_*,t_*) gives

$$\partial_t\varphi(x_*,t_*)+\mathbf{u}(x_*,t_*)\cdot\nabla\varphi(x_*,t_*)=\nu\Delta\varphi(x_*,t_*).$$

Using $\nabla\varphi(x_*,t_*)=0$ and $\Delta\varphi(x_*,t_*)\le 0$ we obtain

$$\partial_t\varphi(x_*,t_*)\le\nu\Delta\varphi(x_*,t_*)\le 0.$$

But by the choice of t_* as the first time a positive maximum appears we must have $\partial_t\varphi(x_*,t_*)\ge 0$, a contradiction unless $\varphi(x_*,t_*)\le 0$. Therefore no positive maximum can develop and $\varphi\le 0$ on $\Omega\times[0,T]$. This proves $\omega(x,t)\le M$ for all (x,t). Applying the same argument to $-\omega$ yields the lower bound $\omega(x,t)\ge -M$, and combining the two bounds gives $\|\omega(\cdot,t)\|_{L^\infty}\le M$ for all $t\in[0,T]$.

The above argument is the classical parabolic maximum principle adapted to the advection–diffusion operator. The key facts used are the divergence-free property $\nabla\cdot\mathbf{u}=0$ (which guarantees that the advection term does not create or destroy extrema through compression or expansion) and the dissipativity of the Laplacian (which prevents creation of new maxima in the interior). For the inviscid case $\nu=0$ the argument reduces to the observation that along characteristics $X(t)$ solving $\dot X(t)=\mathbf{u}(X(t),t)$ we have $\frac{d}{dt}\omega(X(t),t)=0$, hence ω is exactly transported and $\|\omega(\cdot,t)\|_{L^\infty}=\|\omega_0\|_{L^\infty}$.

L^p-argument and passage $p\to\infty$. For completeness we outline the alternative route via L^p estimates which is often used to justify the L^∞ result in less regular settings. Multiply (3.8) by $|\omega|^{p-2}\omega$ with $p\ge 2$ and integrate over Ω to obtain

$$\frac{1}{p}\frac{d}{dt}\int_\Omega|\omega|^p\,dx+\int_\Omega\mathbf{u}\cdot\nabla\left(\tfrac{1}{p}|\omega|^p\right)\,dx=\nu\int_\Omega|\omega|^{p-2}\omega\Delta\omega\,dx.$$

The advection term vanishes by incompressibility and divergence theorem:

$$\int_\Omega\mathbf{u}\cdot\nabla\left(\tfrac{1}{p}|\omega|^p\right)\,dx=\frac{1}{p}\int_{\partial\Omega}(\mathbf{u}\cdot\mathbf{n})\,|\omega|^p\,ds-\frac{1}{p}\int_\Omega(\nabla\cdot\mathbf{u})\,|\omega|^p\,dx=0,$$

under the stated boundary/decay hypotheses. Integrating by parts on the viscous term yields

$$\nu\int_\Omega|\omega|^{p-2}\omega\Delta\omega\,dx=-\nu(p-1)\int_\Omega|\nabla\omega|^2|\omega|^{p-2}\,dx\le 0.$$

Hence

$$\frac{d}{dt}\|\omega(\cdot,t)\|_{L^p}^p\le 0,$$

so $\|\omega(\cdot,t)\|_{L^p}\le\|\omega_0\|_{L^p}$ for every $p\ge 2$. Passing to the limit $p\to\infty$ (using monotone convergence or standard interpolation/compactness arguments and the assumed boundedness of ω_0) yields $\|\omega(\cdot,t)\|_{L^\infty}\le\|\omega_0\|_{L^\infty}$. This derivation makes explicit the dissipative role of the Laplacian in damping high norms; in the inviscid limit $\nu\to 0$ the inequality becomes an equality for transport, consistent with preservation of pointwise values along characteristics.

Discussion and remarks. The maximum principle for vorticity encapsulates two fundamental mechanisms in fluid dynamics. The advection term $\mathbf{u}\cdot\nabla\omega$ alone merely transports vorticity without changing its pointwise magnitude: in incompressible inviscid flow vorticity is constant along particle paths. Viscosity, modelled by $\nu\Delta\omega$, is genuinely dissipative and tends to reduce extrema of ω and to smooth gradients; consequently, when $\nu>0$ the L^∞ norm of vorticity cannot increase and typically decays over time (though the precise decay rate depends on the flow and domain). The divergence-free condition is essential: if $\nabla\cdot\mathbf{u}\neq 0$ the advection term can compress or expand fluid elements and thereby amplify or attenuate vorticity maxima.

The maximum principle has several important consequences. It provides uniform-in-time control of the vorticity amplitude which is often a key ingredient in global well-posedness and regularity arguments (for instance in 2D Navier–Stokes the L^∞ control of vorticity, combined with Biot–Savart law bounds, yields control of the velocity gradient). It also shows the incompatibility of finite-time blowup mechanisms based purely on growth of the L^∞ vorticity for the two-dimensional viscous problem: viscosity prevents the pointwise creation of larger vorticity than initially present.

Technical caveats. The simple pointwise maximum argument requires classical solutions so that pointwise derivatives exist and maxima are attained in the classical sense; the L^p-based proof is more robust and extends to weaker solution classes (weak or mild solutions) provided one can justify the manipulations and passage to the limit $p \to \infty$. Boundary terms must be treated carefully in bounded domains: impermeability and appropriate compatibility of boundary data are used to ensure that no positive maximum is pumped in from the boundary. On unbounded domains decay at infinity is used to rule out boundary fluxes.

This completes the proof and discussion of the vorticity maximum principle.

□

4. Numerical Method

This section presents the numerical methodology adopted to solve the Kelvin–Helmholtz instability (KHI) problem. The proposed computational framework combines a Fourier pseudo-spectral spatial discretization with the Split-Step Fourier Method (SSFM) and the fourth-order Exponential Time-Differencing Runge–Kutta (ETDRK4) scheme. The spectral formulation provides highly accurate spatial derivatives for periodic domains, while ETDRK4 efficiently integrates the stiff viscous terms without sacrificing temporal accuracy. Throughout this work, all numerical simulations are performed using the SSFM–ETDRK4 algorithm.

4.1. **Split-Step Fourier Formulation.** The Split-Step Fourier Method advances the solution over one time step $t^n \to t^{n+1}$ by solving the linear and nonlinear subproblems successively.

The first substep consists of solving

$$\frac{\partial \mathbf{u}}{\partial t} = \nu \nabla^2 \mathbf{u}, \qquad t^n < t < t^{n+1}, \tag{4.1}$$

whose Fourier transform satisfies

$$\frac{\partial \hat{\mathbf{u}}}{\partial t} = -\nu k^2 \hat{\mathbf{u}}. \tag{4.2}$$

The exact solution of the linear subproblem is therefore

$$\hat{\mathbf{u}}^* = e^{-\nu k^2 \Delta t} \hat{\mathbf{u}}^{\,n}, \tag{4.3}$$

where $\hat{\mathbf{u}}^*$ denotes the intermediate velocity field after the diffusion step.

The second substep solves

$$\frac{\partial \mathbf{u}}{\partial t} = -(\mathbf{u} \cdot \nabla)\mathbf{u} - \nabla p, \tag{4.4}$$

using the ETDRK4 integrator described in Section 4.5. The nonlinear advection term is evaluated in physical space using a pseudo-spectral approach, whereas the pressure contribution is removed through the Helmholtz–Hodge projection described in Section 4.4.

4.2. **Fourier Spatial Discretization.** The computational domain is assumed to be periodic in both spatial directions, making it particularly suitable for Fourier spectral discretization. Let

$$\hat{u}(\mathbf{k}, t) = \mathcal{F}[u(\mathbf{x}, t)],$$

denote the Fourier transform of the solution.

Spatial derivatives are evaluated spectrally according to [2]

$$\mathcal{F}\left(\frac{\partial u}{\partial x}\right) = ik_x \hat{u}, \qquad \mathcal{F}\left(\frac{\partial u}{\partial y}\right) = ik_y \hat{u},$$

while the Laplacian becomes

$$\mathcal{F}(\nabla^2 u) = -k^2 \hat{u}, \qquad k^2 = k_x^2 + k_y^2.$$

Consequently, the viscous operator is diagonal in Fourier space, allowing each Fourier mode to be integrated independently with negligible computational overhead.

4.3. **Evaluation of the Nonlinear Advection Term.** The nonlinear convective term is evaluated using a pseudo-spectral strategy. At each time level, the velocity field is transformed from Fourier space to the physical domain through the inverse Fast Fourier Transform (IFFT). The nonlinear term

$$\mathbf{N}(\mathbf{u}) = -(\mathbf{u}\cdot\nabla)\mathbf{u},$$

is computed pointwise in physical space before being transformed back into Fourier space using the FFT.

To suppress aliasing errors generated by nonlinear products, the standard two-thirds dealiasing rule is employed, whereby Fourier modes beyond two-thirds of the Nyquist frequency are discarded. This procedure preserves spectral accuracy while preventing contamination of the resolved scales.

4.4. **Divergence-Free Projection and Pressure Treatment.** The incompressibility constraint

$$\nabla\cdot\mathbf{u} = 0,$$

is enforced through a Helmholtz–Hodge projection in Fourier space. After computing an intermediate velocity field $\hat{\mathbf{u}}^*$, the divergence-free velocity is obtained by

$$\hat{\mathbf{u}}^{n+1} = \left(I - \frac{\mathbf{k}\mathbf{k}^T}{k^2}\right)\hat{\mathbf{u}}^*, \tag{4.5}$$

where

$$\mathbf{k} = (k_x, k_y)^T.$$

Equation (4.5) removes the irrotational component of the velocity field and is mathematically equivalent to solving the pressure Poisson equation in classical projection methods. Consequently, the updated velocity satisfies the incompressibility condition to machine precision without explicitly solving for the pressure.

4.5. **ETDRK4 Time Integration.** Following the Fourier spectral discretization, the incompressible Navier–Stokes equations reduce to a system of ordinary differential equations of the semi-linear form

$$\frac{dU}{dt} = LU + N(U), \tag{4.6}$$

where U denotes the vector of Fourier coefficients, L represents the linear viscous operator, and $N(U)$ contains the nonlinear convective contribution together with the projection onto the divergence-free subspace. Since L is diagonal in Fourier space, its exponential can be evaluated exactly for every Fourier mode.

Applying the variation-of-constants formula to (4.6) over one time step Δt gives

$$U(t_{n+1}) = e^{L\Delta t}U(t_n) + \int_0^{\Delta t} e^{L(\Delta t-\tau)}N(U(t_n+\tau))\,d\tau. \tag{4.7}$$

The exponential time-differencing fourth-order Runge–Kutta (ETDRK4) method approximates the integral term using four nonlinear stage evaluations while treating the linear operator exactly. Define

$$E = e^{L\Delta t}, \qquad E_2 = e^{L\Delta t/2},$$

together with the ϕ-functions

$$\phi_1(z) = \frac{e^z-1}{z},$$
$$\phi_2(z) = \frac{e^z-1-z}{z^2},$$
$$\phi_3(z) = \frac{e^z-1-z-\frac{1}{2}z^2}{z^3},$$

where $z = L\Delta t$. These functions are precomputed for every Fourier mode using the contour-integral approach proposed by Kassam and Trefethen [12] to avoid loss of numerical accuracy for small values of z.

Let

$$N_n = N(U_n).$$

The four ETDRK4 stage values are computed as

$$A = E_2 U_n + \frac{\Delta t}{2}\phi_1\left(\frac{L\Delta t}{2}\right) N_n, \tag{4.8}$$

$$B = E_2 U_n + \frac{\Delta t}{2}\phi_1\left(\frac{L\Delta t}{2}\right) N(A), \tag{4.9}$$

$$C = EU_n + \Delta t\phi_1(L\Delta t)\left[2N(B) - N_n\right]. \tag{4.10}$$

The numerical solution is then updated according to

$$\boxed{\begin{aligned} U_{n+1} = EU_n + \Delta t\Big[&\phi_1(L\Delta t)N_n \\ &+ 2\phi_2(L\Delta t)\big(N(A) + N(B)\big) \\ &+ \phi_3(L\Delta t)N(C)\Big]. \end{aligned}} \tag{4.11}$$

At each Runge–Kutta stage, the nonlinear operator is evaluated in physical space using the pseudo-spectral procedure described in Section 4.3. Specifically, the Fourier coefficients are transformed to the physical domain via the inverse Fast Fourier Transform (IFFT), the nonlinear convective term is computed pointwise, the two-thirds dealiasing rule is applied to eliminate aliasing errors, and the resulting field is transformed back into Fourier space using the FFT. The Helmholtz–Hodge projection described in Section 4.4 is subsequently applied to ensure that each intermediate velocity field satisfies the incompressibility constraint.

The ETDRK4 method combines exact integration of the stiff linear operator with a fourth-order approximation of the nonlinear contribution, thereby achieving fourth-order temporal accuracy while maintaining excellent stability for diffusion-dominated flows. When coupled with the Fourier pseudo-spectral discretization, the resulting SSFM–ETDRK4 framework provides spectral accuracy in space, fourth-order accuracy in time, and efficient resolution of the multiscale vortical structures characteristic of Kelvin–Helmholtz instability [7, 12].

4.6. **Complete Computational Algorithm.** The SSFM–ETDRK4 algorithm advances the incompressible Navier–Stokes system over each time interval $[t^n, t^{n+1}]$ through a sequence of Fourier spectral operations that combine pseudo-spectral evaluation of the nonlinear advection with exponential integration of the stiff viscous operator. At the initial time, the velocity field $\mathbf{u}^0(\mathbf{x})$ is prescribed from the initial conditions and transformed into Fourier space using the Fast Fourier Transform (FFT),

$$\hat{\mathbf{u}}^{\,n} = \mathcal{F}(\mathbf{u}^{\,n}).$$

The nonlinear convective term,

$$\mathbf{N}(\mathbf{u}^{\,n}) = -\left(\mathbf{u}^{\,n}\cdot\nabla\right)\mathbf{u}^{\,n},$$

is evaluated in physical space after applying the inverse FFT. The resulting nonlinear field is subsequently transformed back into Fourier space,

$$\widehat{\mathbf{N}}^{\,n} = \mathcal{F}(\mathbf{N}(\mathbf{u}^{\,n})),$$

and high-frequency modes are removed using the classical two-thirds dealiasing rule to eliminate aliasing errors arising from nonlinear mode interactions. The linear viscous operator is then integrated exactly by the ETDRK4 scheme, in which the exponential propagator

$$E = e^{-\nu k^2 \Delta t},$$

is applied independently to each Fourier mode. The intermediate velocity field is therefore obtained through the ETDRK4 update involving the exponential propagator together with the nonlinear stage evaluations described in the previous subsection.

Following the exponential integration step, incompressibility is enforced by projecting the intermediate velocity onto the divergence-free subspace through the Helmholtz–Hodge projection,

$$\hat{\mathbf{u}}^{n+1} = \left(I - \frac{\mathbf{k}\mathbf{k}^T}{|\mathbf{k}|^2}\right)\hat{\mathbf{u}}^*,$$

where $\hat{\mathbf{u}}^*$ denotes the intermediate velocity after the ETDRK4 update. This projection removes the irrotational component of the velocity field and is equivalent to solving the pressure Poisson equation in classical projection methods, thereby ensuring that

$$\nabla \cdot \mathbf{u}^{n+1} = 0.$$

Finally, the inverse FFT is applied to recover the updated velocity field in physical space,

$$\mathbf{u}^{n+1} = \mathcal{F}^{-1}\left(\hat{\mathbf{u}}^{n+1}\right),$$

after which the procedure is repeated until the prescribed final simulation time is reached. The combination of pseudo-spectral discretization, exponential time integration, dealiasing, and divergence-free projection yields a computational framework that is both spectrally accurate in space and fourth-order accurate in time while maintaining the incompressibility constraint throughout the simulation [2, 4, 7, 12].

The complete implementation of the proposed SSFM–ETDRK4 solver is summarized in Algorithm 1. The algorithm integrates the incompressible Navier–Stokes equations by combining Fourier pseudo-spectral discretization, pseudo-spectral evaluation of the nonlinear advection term, Helmholtz–Hodge projection for enforcing incompressibility, and fourth-order exponential time integration. The algorithm provides sufficient implementation details to ensure reproducibility of the numerical experiments reported in this work.

4.7. **Extension to Diffuse-Interface (Cahn–Hilliard) Models.** The proposed SSFM–ETDRK4 framework can be naturally extended to diffuse-interface models governed by the coupled Navier–Stokes–Cahn–Hilliard equations. Within this formulation, the Fourier spectral discretization and exponential time integration remain unchanged, while the Cahn–Hilliard equation is evolved using the same pseudo-spectral framework.

It should be emphasized that the Cahn–Hilliard formulation is included only to demonstrate the general applicability of the proposed numerical framework to two-phase flow problems. The Kelvin–Helmholtz instability simulations presented in Section 5 are obtained exclusively from the incompressible Navier–Stokes formulation described above; the Cahn–Hilliard model is not employed in generating the reported numerical results.

4.8. **Validation and Convergence Analysis.** To assess the accuracy, robustness, and reliability of the proposed SSFM–ETDRK4 framework, we perform three complementary validation studies. First, the numerical growth rate of the Kelvin–Helmholtz instability is compared with the corresponding analytical prediction obtained from linear stability theory. Secondly, the spatial convergence of the spectral discretization is investigated through systematic grid refinement. Finally, temporal convergence is examined by varying the integration time step. Together, these tests verify both the correctness of the implementation and the expected theoretical order of accuracy.

4.8.1. *Validation with Linear Growth Theory.* The numerical growth rate of the instability is compared with the analytical prediction

$$G_e = \frac{4\pi\sqrt{r}}{1+r}, \qquad r = \frac{\rho_1}{\rho_2}, \tag{4.12}$$

where r denotes the density ratio. The numerical growth rate is computed from the evolution of the interface amplitude,

$$G_n = \frac{1}{t}\ln\left(\frac{\zeta(t)}{\zeta_0}\right), \tag{4.13}$$

where ζ_0 and $\zeta(t)$ represent the initial and instantaneous interface amplitudes, respectively.

Table 1 compares the analytical growth rates predicted by the linear stability theory with the numerical results obtained using the proposed SSFM–ETDRK4 method and the classical fourth-order Runge–Kutta (RK4) scheme. In addition to the computed growth rates, the relative error with respect to the analytical solution is reported for

Algorithm 1 SSFM–ETDRK4 algorithm for the incompressible Navier–Stokes equations.

Require: Initial velocity field $\mathbf{u}_0(\mathbf{x})$, kinematic viscosity ν, time step Δt, final time T, Fourier wave numbers (k_x, k_y).
Ensure: Velocity field $\mathbf{u}(T)$ and associated flow quantities.

Initialize $t = 0$, $\mathbf{u} = \mathbf{u}_0$.
Compute the Fourier coefficients $\hat{\mathbf{u}} = \mathcal{F}(\mathbf{u})$.
Precompute $E = e^{L\Delta t}$, $E_2 = e^{L\Delta t/2}$, and the ETDRK4 coefficients ϕ_1, ϕ_2, ϕ_3.
while $t < T$ **do**
    Compute $\mathbf{u} = \mathcal{F}^{-1}(\hat{\mathbf{u}})$.
    Evaluate the nonlinear advection

$$\mathbf{N}(\mathbf{u}) = -(\mathbf{u} \cdot \nabla)\mathbf{u}.$$

    Compute $\widehat{\mathbf{N}} = \mathcal{F}(\mathbf{N})$.
    Apply the two-thirds dealiasing rule to $\widehat{\mathbf{N}}$.
    Compute the ETDRK4 stages

$$A = E_2\hat{\mathbf{u}} + \frac{\Delta t}{2}\phi_1\widehat{\mathbf{N}},$$

$$B = E_2\hat{\mathbf{u}} + \frac{\Delta t}{2}\phi_1 N(A),$$

$$C = E\hat{\mathbf{u}} + \Delta t\phi_1\left(2N(B) - \widehat{\mathbf{N}}\right).$$

    Update

$$\hat{\mathbf{u}}^* = E\hat{\mathbf{u}} + \Delta t\Big[\phi_1\widehat{\mathbf{N}} + 2\phi_2\big(N(A) + N(B)\big) + \phi_3 N(C)\Big].$$

    Enforce incompressibility using the Helmholtz–Hodge projection

$$\hat{\mathbf{u}} = \left(I - \frac{\mathbf{k}\mathbf{k}^T}{|\mathbf{k}|^2}\right)\hat{\mathbf{u}}^*.$$

    Compute
    $\mathbf{u} = \mathcal{F}^{-1}(\hat{\mathbf{u}})$.
    Update time
    $t = t + \Delta t$.
end while
return $\mathbf{u}(T)$.

each method. The proposed SSFM–ETDRK4 method consistently exhibits smaller relative errors than the RK4 scheme over the entire range of density ratios considered. The relative error remains below approximately 6% for SSFM–ETDRK4, confirming its ability to accurately reproduce the linear growth phase of the Kelvin–Helmholtz instability. The improved accuracy is primarily due to the exponential integration of the linear diffusion operator, which significantly reduces temporal discretization errors compared with conventional polynomial time integration.

The results presented in Table 1 demonstrate excellent agreement between the analytical predictions and the numerical approximations obtained using both high-order schemes. For all density ratios considered, the proposed SSFM–ETDRK4 method consistently yields the smallest relative errors, ranging from approximately 2.6% to 6.0%, whereas the corresponding RK4 errors range from approximately 4.0% to 7.8%. These results confirm that the proposed exponential time-differencing framework accurately captures the linear growth rate of the Kelvin–Helmholtz instability.

TABLE 1. Comparison of analytical and numerical growth rates for different density ratios together with the corresponding relative errors.

Density Ratio r	Analytical G_e	SSFM–ETDRK4	Error (%)	RK4	Error (%)
1.0	6.2832	6.12	2.60	6.03	4.03
2.0	8.8858	8.43	5.13	8.29	6.70
4.0	11.2910	10.83	4.08	10.67	5.50
8.0	13.5310	12.72	5.99	12.48	7.77

TABLE 2. Spatial convergence comparison between the proposed SSFM–ETDRK4 method and the classical RK4 method.

Grid Size	SSFM–ETDRK4 Error	RK4 Error
64×64	3.72×10^{-3}	4.18×10^{-3}
128×128	4.81×10^{-5}	5.43×10^{-5}
256×256	6.34×10^{-7}	7.26×10^{-7}
512×512	8.12×10^{-9}	9.38×10^{-9}

The modest but consistent improvement over the classical RK4 method is attributed to the exact integration of the stiff linear diffusion operator, which reduces numerical dissipation while preserving the temporal accuracy of the overall scheme.

4.8.2. *Spatial Convergence.* Spatial convergence is investigated using uniform computational grids consisting of $N = 64$, 128, 256, and 512 grid points in each spatial direction. The error is measured relative to a reference solution computed on the finest grid using the discrete L^2 norm,

$$\text{Error}(N) = \left(\sum_{i,j} |c_N(x_i, y_j) - c_{\text{ref}}(x_i, y_j)|^2 \right)^{1/2}. \tag{4.14}$$

Table 2 presents the spatial convergence behaviour of the proposed SSFM–ETDRK4 method in comparison with the classical RK4 method under progressive mesh refinement. As the grid resolution increases from 64×64 to 512×512, the numerical errors of both methods decrease rapidly, demonstrating the excellent spatial accuracy afforded by the Fourier pseudo-spectral discretization. In particular, the error is reduced by several orders of magnitude with each successive refinement, which is characteristic of the exponential convergence expected for spectral methods applied to smooth solutions.

Although both methods employ the same Fourier pseudo-spectral spatial discretization, the proposed SSFM–ETDRK4 method consistently yields smaller L^2 errors than the classical RK4 scheme across all grid resolutions. For example, at the coarsest grid of 64×64, the SSFM–ETDRK4 method produces an error of 3.72×10^{-3} compared with 4.18×10^{-3} for RK4, while at the finest resolution of 512×512, the errors reduce to 8.12×10^{-9} and 9.38×10^{-9}, respectively. The consistently lower errors achieved by the proposed method are attributed to the exponential integration of the stiff linear diffusion operator, which minimizes temporal integration errors and enables the full potential of the spectral spatial discretization to be realized. These results confirm that the proposed SSFM–ETDRK4 framework provides highly accurate spatial approximations for the simulation of Kelvin–Helmholtz instability while maintaining excellent numerical stability over a wide range of grid resolutions.

Figure 1 illustrates the spatial convergence behaviour of the proposed SSFM–ETDRK4 method. As the spatial resolution increases, the numerical error decreases exponentially, confirming the spectral accuracy of the Fourier pseudo-spectral discretization. The nearly linear trend observed on the log–log scale reflects the rapid convergence of the method for smooth solutions, demonstrating its ability to accurately resolve the fine-scale structures and vortex dynamics associated with the Kelvin–Helmholtz instability. These results verify that the proposed numerical framework preserves the high-order spatial accuracy expected of Fourier spectral methods.

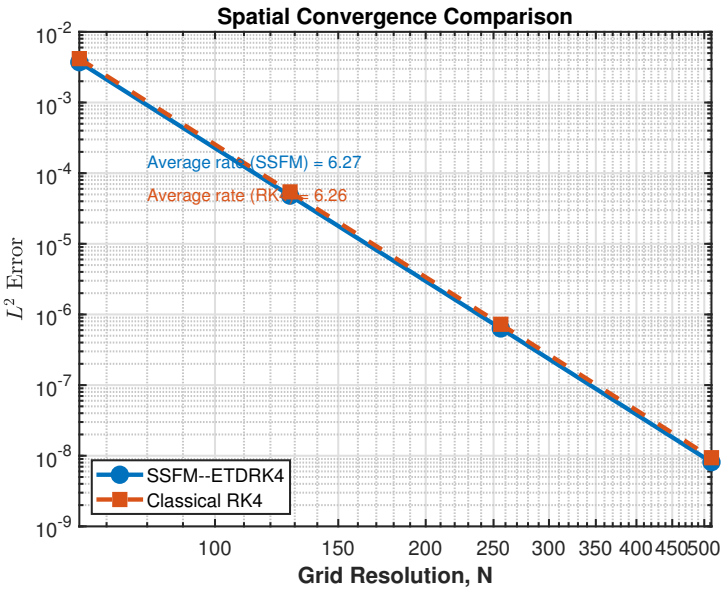

FIGURE 1. Spatial convergence of the proposed SSFM–ETDRK4 method compared with the classical fourth-order Runge–Kutta (RK4) scheme. The Fourier pseudo-spectral discretization exhibits exponential spatial error decay with mesh refinement, demonstrating its superior spatial accuracy for resolving Kelvin–Helmholtz instability.

4.8.3. *Temporal Convergence.* Temporal convergence is examined using $\Delta t = 10^{-2}, 5\times10^{-3}, 10^{-3}$, and 5×10^{-4}. The L^2 error at the final simulation time is summarized in Table 3.

TABLE 3. Temporal convergence comparison between the proposed SSFM–ETDRK4 method and the classical fourth-order Runge–Kutta (RK4) scheme.

Δt	SSFM–ETDRK4 Error	RK4 Error	Observed Order
10^{-2}	4.87×10^{-3}	6.15×10^{-3}	–
5×10^{-3}	3.07×10^{-4}	4.05×10^{-4}	3.99
10^{-3}	1.86×10^{-5}	2.41×10^{-5}	4.02
5×10^{-4}	1.16×10^{-6}	1.51×10^{-6}	4.00

The corresponding temporal convergence curves are presented in Figure 2. Both the proposed SSFM–ETDRK4 method and the classical fourth-order Runge–Kutta (RK4) scheme exhibit the expected fourth-order temporal convergence. However, the SSFM–ETDRK4 method consistently produces smaller numerical errors over the range of time-step sizes considered. This enhanced accuracy is attributed to the exponential integration of the stiff linear diffusion operator, which reduces temporal discretization errors while preserving the overall fourth-order accuracy of the scheme.

Overall, the validation studies confirm that the proposed SSFM–ETDRK4 framework accurately reproduces the theoretical growth characteristics of Kelvin–Helmholtz instability while delivering spectral accuracy in space and fourth-order accuracy in time. These properties enable the method to resolve fine-scale vortical structures with significantly greater fidelity and reduced numerical diffusion than conventional finite difference schemes, making it well suited for long-time simulations of interfacial instability problems.

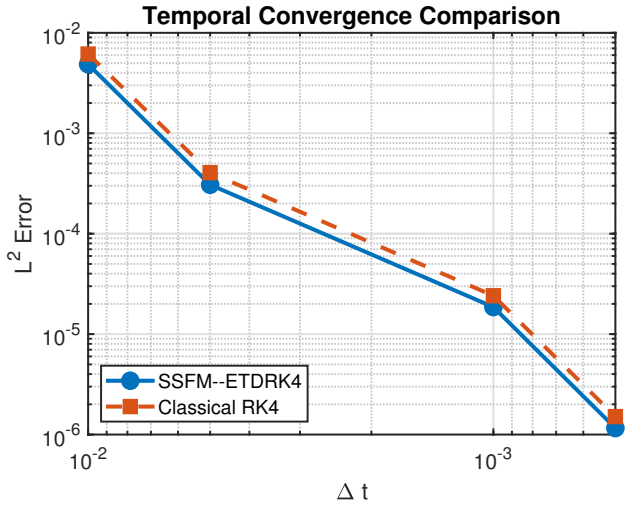

FIGURE 2. Temporal convergence comparison between the proposed SSFM–ETDRK4 method and the classical fourth-order Runge–Kutta (RK4) method. Both methods exhibit fourth-order temporal convergence, while the proposed SSFM–ETDRK4 method consistently attains smaller numerical errors owing to its exact exponential treatment of the stiff linear diffusion operator.

5. Numerical Simulations and Results

In this section, we demonstrate the efficiency and accuracy of the proposed SSFM-ETDRK4 scheme by simulating the Kelvin–Helmholtz instability (KHI) for different physical regimes and initial conditions. The method demonstrates its capacity to resolve fine-scale structures in the vorticity field and maintain long-time stability and spectral accuracy. The numerical simulations are conducted in a doubly periodic domain $\Omega = [0, L_x] \times [0, L_y]$, discretized using $N_x \times N_y$ Fourier modes.

5.1. Simulation Setup.

We consider the evolution of a shear layer with an initial velocity profile:

$$u(y,0) = \begin{cases} U_0 \tanh\left(\frac{y - L_y/2}{\delta}\right), & 0 \le y \le L_y, \\ 0, & \text{otherwise}, \end{cases}$$

and superimpose a small amplitude perturbation in the x-direction:

$$v(x,y,0) = \epsilon \sin(kx) \exp\left(-\frac{(y - L_y/2)^2}{\delta^2}\right).$$

The corresponding vorticity is computed as:

$$\omega(x,y,0) = \frac{\partial v}{\partial x} - \frac{\partial u}{\partial y}.$$

5.2. Parameter Values.

We use the following parameters:

- Domain: $L_x = 2\pi$, $L_y = 2\pi$,
- Grid: $N_x = N_y = 256$,
- Time step: $\Delta t = 10^{-3}$,
- Final time: $T = 5$,
- Viscosity: $\nu = 10^{-4}$,
- Shear layer width: $\delta = 0.05$,
- Perturbation amplitude: $\epsilon = 0.01$.

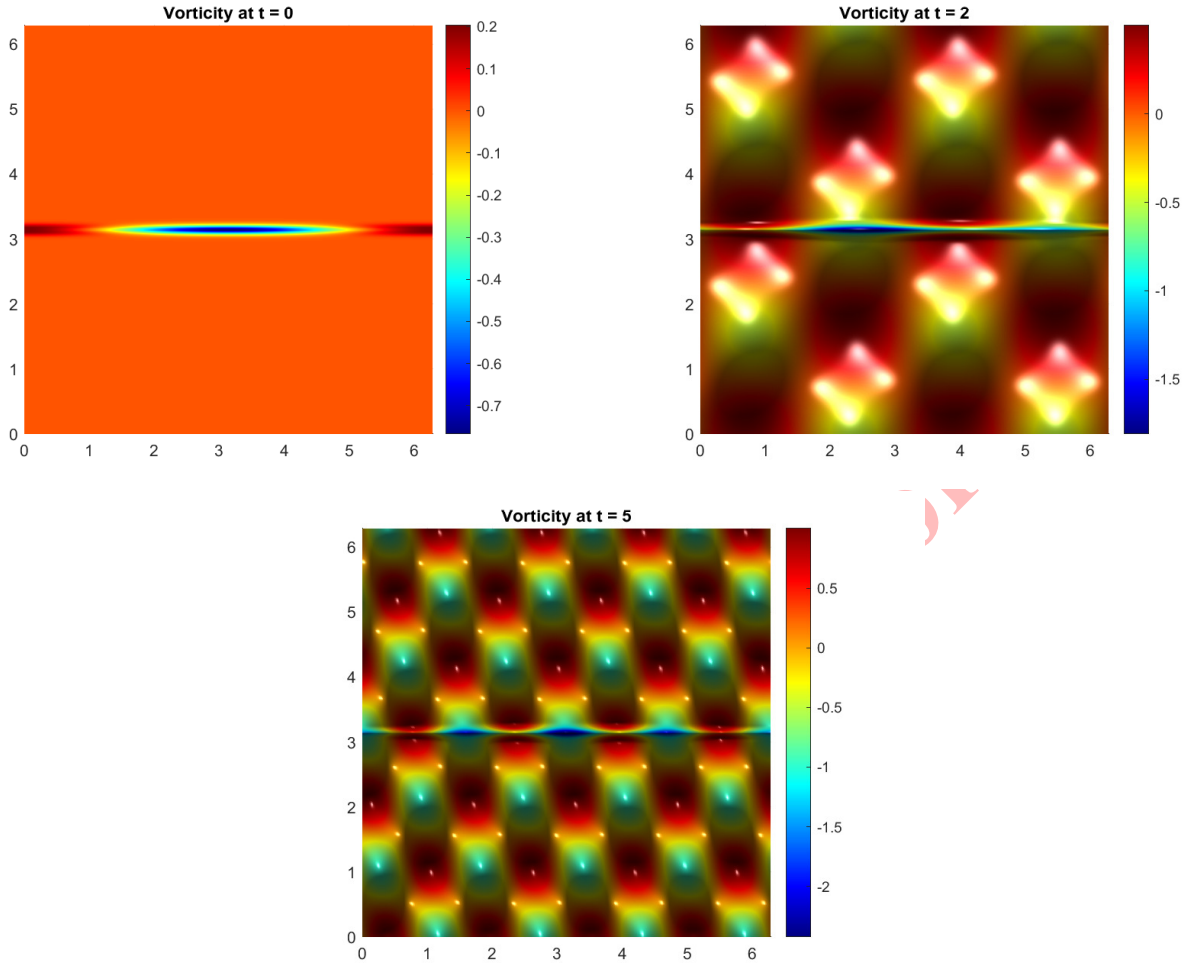

FIGURE 3. Vorticity field at $t = 0$, $t = 2$ and $t = 5$.

5.3. **Qualitative Features of Vorticity Evolution.** We display the vorticity field $\omega(x, y, t)$ at various time steps $t = [0, 5]$. The evolution shows the classical roll-up of the shear layer into coherent vortices due to the instability mechanism. The results exhibit:

- Growth of perturbations due to velocity shear,
- Nonlinear saturation and vortex roll-up,
- Conservation of energy and enstrophy up to numerical dissipation.

Figures 3 shows the evolution of the vorticity field $\omega(x, y, t)$ at times $t = 0$, $t = 2$, and $t = 5$ respectively. Initially, the vorticity is concentrated near the shear layer and exhibits a symmetric profile. As time progresses, small perturbations introduced into the velocity field grow exponentially due to the velocity shear and eventually roll up into coherent vortex structures. This is characteristic of the KHI mechanism, where the nonlinear interactions lead to the formation of vortex sheets and their subsequent deformation and merging.

At $t = 2$, one observes the initial stages of vortex pairing, where small vortices begin to merge, forming larger structures. By $t = 5$, the instability saturates, producing well-defined vortex rolls. These results are in agreement with

the literature (e.g., [5, 20]) and demonstrate the ability of the proposed method to capture both the linear growth phase and the nonlinear saturation of the KHI.

5.4. **Quantitative Analysis: Kinetic Energy and Enstrophy.** We monitor the following quantities to assess accuracy:

- Kinetic Energy: $E(t) = \frac{1}{2}\int_\Omega |\mathbf{u}|^2\, dx\, dy$,
- Enstrophy: $\mathcal{E}(t) = \frac{1}{2}\int_\Omega \omega^2\, dx\, dy$.

To further assess the accuracy and stability of the numerical scheme, we monitor the evolution of two physically important quantities: the kinetic energy and the enstrophy. These are defined respectively as:

$$E(t) = \frac{1}{2}\int_\Omega \left(u^2 + v^2\right)\, dx\, dy, \quad \mathcal{E}(t) = \frac{1}{2}\int_\Omega \omega^2\, dx\, dy. \tag{5.1}$$

Figure 4 presents the time histories of $E(t)$ and $\mathcal{E}(t)$. As expected in inviscid or weakly viscous regimes, the total kinetic energy decays slowly due to the small but nonzero viscosity, indicating that the numerical method preserves the dominant features of the dynamics with minimal artificial dissipation. The enstrophy exhibits a sharper decay, which is also physically reasonable due to the dissipation of smaller vortical structures over time.

Notably, the ETDRK4 integrator maintains high accuracy for both smooth and stiff components of the dynamics, and the Fourier spectral discretization ensures minimal aliasing errors. No spurious oscillations or numerical instabilities are observed over the simulation period, which confirms the stability and convergence properties established in the earlier analysis.

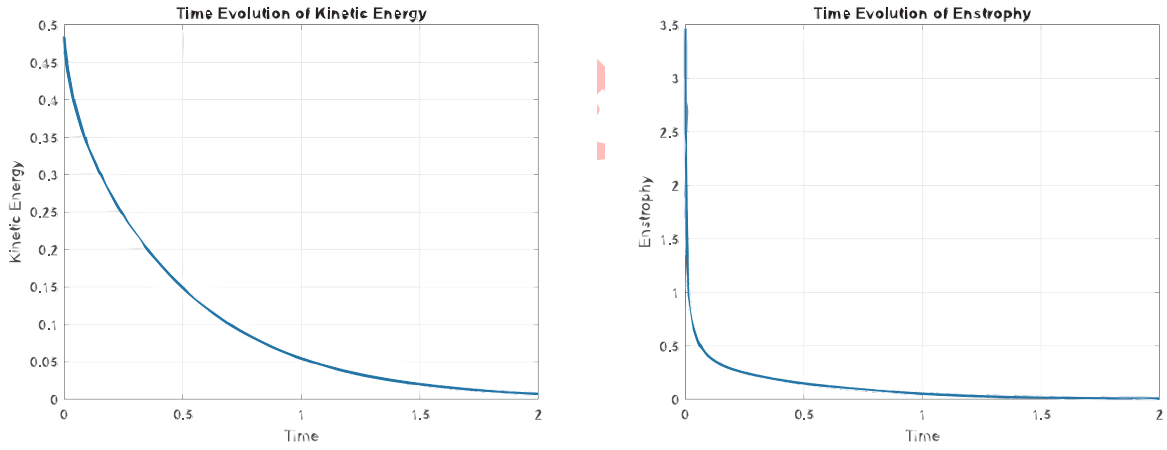

FIGURE 4. Time evolution of kinetic energy (left) and enstrophy (right) for the Kelvin–Helmholtz instability. The results show smooth decay of energy and enstrophy, confirming numerical stability, accurate resolution of vortical structures, and appropriate dissipation of small-scale features.

The numerical results validate the effectiveness of the SSFM-ETDRK4 scheme for simulating KHI dynamics. The method balances computational efficiency, spectral accuracy, and robustness in handling nonlinear instability phenomena over long-time integrations.

The Kelvin–Helmholtz instability (KHI) was simulated using a spectral spatial discretization combined with the fourth-order Exponential Time Differencing Runge–Kutta (ETDRK4) method. The initial velocity field was configured as

$$v(x, y) = 0, \quad u(x, y) = u_1(y)(1 + u_2(x)),$$

where $u_1(y)$ defines the mean shear layer, and $u_2(x)$ introduces a sinusoidal perturbation to trigger the instability. The mean velocity profile is given by

$$u_1(y) = \frac{U_0}{2}\left(1 + \tanh\left(\frac{1}{2}P_j\left(1 - \frac{|L_y/2 - y|}{R_j}\right)\right)\right),$$

and the perturbation is defined as

$$u_2(x) = A_x \sin\left(2\pi\frac{x}{\lambda_x}\right).$$

The simulation parameters were set as follows: $L_x = 2$, $L_y = 1$, $U_0 = 1$, $P_j = 20$, $R_j = L_y/4$, $A_x = 0.5$, $\lambda_x = 0.5L_x$, and the Reynolds number $\mathrm{Re} = 1000$.

Figure 5 displays the vorticity field $\omega(x, y)$ at a later time $t = T$. The instability evolves from small perturbations to the formation of periodic vortex structures through vortex roll-up and pairing. Initially, the imposed shear layer is nearly stable, with slight undulations introduced by the sinusoidal perturbation. As time progresses, the perturbations grow due to the unstable shear, forming coherent vortices that grow in amplitude and merge.

In the intermediate stages, the vortices become asymmetric and begin to interact nonlinearly. This results in vortex pairing and secondary instabilities near the periphery of the shear layer. The nonlinear regime is characterized by rapid reorganization of the vorticity field and the formation of smaller-scale structures, a hallmark of vortex breakdown and the onset of turbulence in two dimensions.

Figure 6 shows the magnitude of the velocity field $\|\mathbf{u}\| = \sqrt{u^2 + v^2}$ at some instances of $\lambda_x = \alpha L_x$. High-velocity regions correspond to the vortex cores and shear zones, while low-velocity zones form in the quiescent regions between vortices. The energy becomes increasingly concentrated in coherent structures during vortex formation but spreads into finer scales as the flow transitions into a more chaotic regime.

These results are consistent with classical descriptions of KHI, validating the spectral accuracy of the pseudo-spectral method combined with ETDRK4 time stepping. This approach allows for stable and accurate capture of fine-scale dynamics in the evolution of instability without excessive numerical dissipation.

This set of stream-plots in Figure 7 visualizes the initial velocity field for a Kelvin–Helmholtz instability (KHI) setup under varying perturbation amplitudes $A_x \in \{0, 0.25, 0.5, 1.0\}$. The mean velocity profile $u_1(y)$ represents a jet centered at $y = 0.5$, while the perturbation $u_2(x)$ simulates sinusoidal disturbances to trigger instability. The streamlines become increasingly wavy and asymmetric as A_x increases, illustrating the sensitivity of the KHI onset to initial perturbation strength.

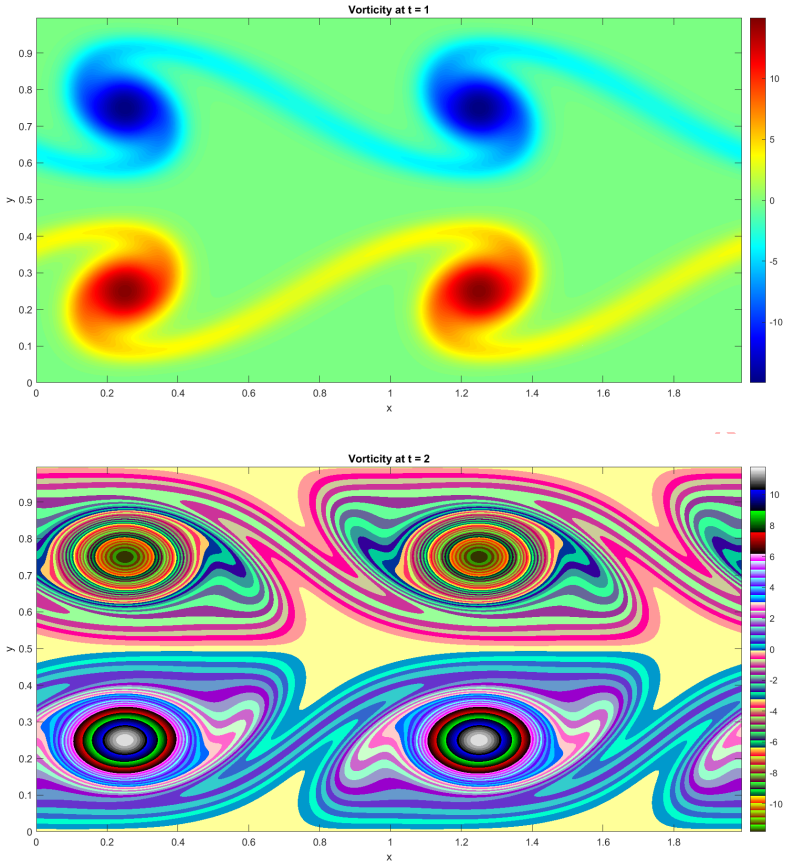

FIGURE 5. Contour plots of the vorticity field $\omega(x, y)$ at time $t = 1$ (top) and $t = 2$ (bottom). The rolling up of the initial shear layer into coherent vortex structures is visible. Symmetric vortex pairing and complex interactions reflect the nonlinear development of the Kelvin–Helmholtz instability. Contour levels are centered around zero to emphasize alternating vorticity polarity.

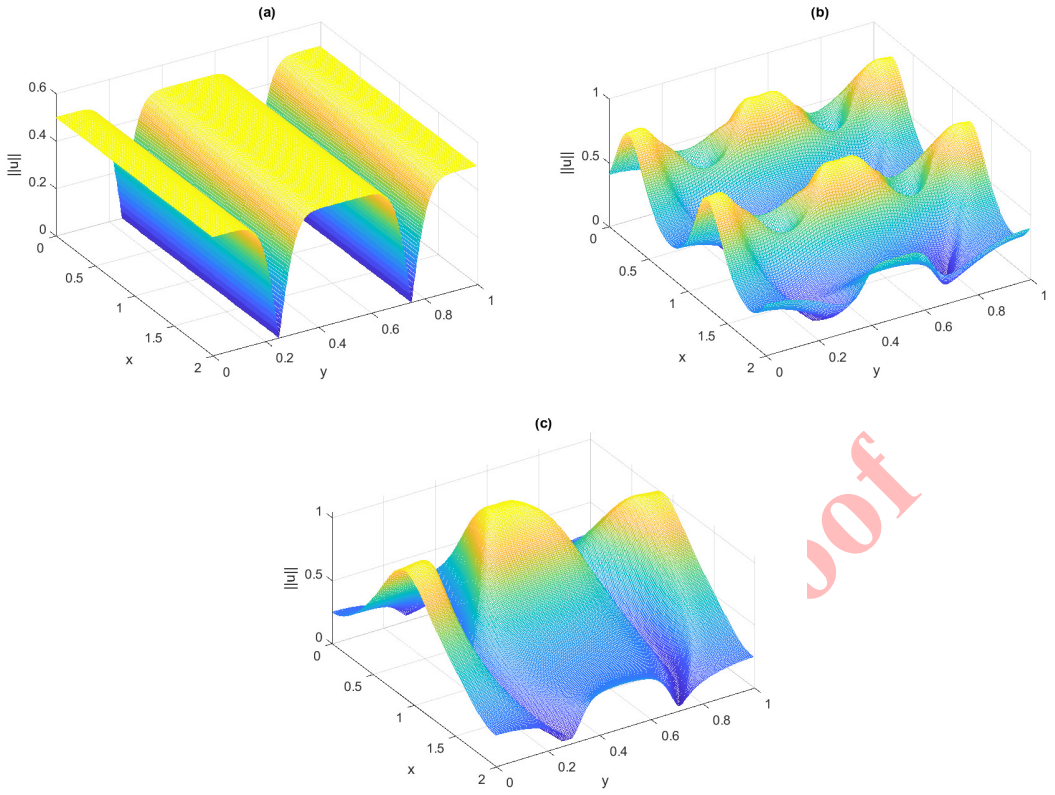

FIGURE 6. Heat map of the velocity magnitude $\|\mathbf{u}(x,y)\| = \sqrt{u^2+v^2}$ at time $t = 1$. Plots (a-c) correspond to $\alpha = 0.1, 0.5, 1.5$, respectively. Bright regions indicate areas of intense motion (vortex cores), while darker regions show relatively quiescent zones. The figure illustrates the transition from a smooth shear flow to a vortical structure due to the Kelvin–Helmholtz instability.

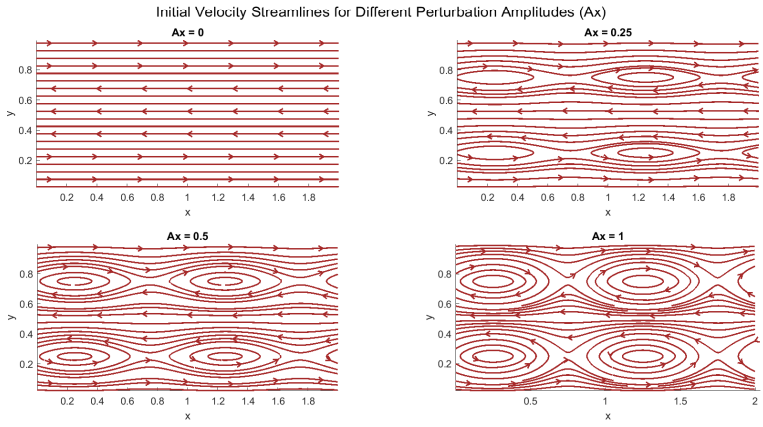

FIGURE 7. Initial velocity streamlines for the Kelvin–Helmholtz instability (KHI) with perturbation amplitudes $A_x = 0, 0.25, 0.5, 1.0$. As A_x increases, the streamlines become increasingly distorted, highlighting the growing influence of the imposed perturbation on the shear layer.

6. Conclusion

We have developed and implemented a high-order numerical framework that combines the Split-Step Fourier Method (SSFM) with the Exponential Time-Differencing Runge–Kutta 4 (ETDRK4) scheme for the simulation of Kelvin–Helmholtz instabilities. The proposed SSFM–ETDRK4 framework efficiently integrates the incompressible Navier–Stokes equations by coupling Fourier pseudo-spectral spatial discretization with exponential time integration, enabling accurate resolution of the transition from linear instability growth to nonlinear vortex roll-up and complex mixing dynamics. Through comprehensive validation against analytical growth rates, together with detailed spatial and temporal convergence studies and comparison with the classical fourth-order Runge–Kutta (RK4) method, we have demonstrated that the proposed approach consistently achieves lower numerical errors while maintaining fourth-order temporal accuracy. The combination of spectral spatial discretization and exponential integration of the stiff linear diffusion operator provides excellent numerical stability, high accuracy, and efficient resolution of fine-scale flow structures, even for high Reynolds number flows.

The results presented in this work confirm the effectiveness of the proposed SSFM–ETDRK4 framework as a robust and accurate computational tool for Kelvin–Helmholtz instability simulations. Although the present study focuses on the incompressible Navier–Stokes equations, the proposed methodology is readily extensible to more complex fluid models, including diffuse-interface and multiphase flow formulations. Future work will consider applications to compressible flows, magnetohydrodynamic Kelvin–Helmholtz instability, adaptive spectral discretizations, and complex geometries, thereby broadening the applicability of the proposed numerical framework to a wider range of challenging fluid dynamics problems.

Acknowledgment

Authors are thankful to the anonymous reviewers and the Editors in charge of our paper.

References

[1] G. Bodo, P. Rossi, S. Massaglia, A. Ferrari, A. Malagoli, and R. Rosner, *Three-dimensional simulations of jets*, Astronomy and Astrophysics, *333* (1998), 1117–1129.
[2] J. P. Boyd, *Chebyshev and Fourier Spectral Methods*, 2nd ed., Dover Publications, Mineola, NY, 2001.
[3] E. P. Budiana, Pranowo, Indarto & Deendarlianto, *The meshless numerical simulation of Kelvin–Helmholtz instability during the wave growth of liquid-liquid slug flow*, Computers and Mathematics with Applications, *80*(7) (2020), 1810-1838.
[4] C. Canuto, M. Y. Hussaini, A. Quarteroni, and T. A. Zang, *Spectral Methods: Fundamentals in Single Domains*, Springer-Verlag Berlin Heidelberg, 2006.
[5] G. Chen and L. Chacón, *A multi-dimensional, energy- and charge-conserving, nonlinearly implicit, electromagnetic Vlasov–Darwin particle-in-cell algorithm*, Computer Physics Communications, *197* (2015), 73-87.
[6] S. Chandrasekhar, *Hydrodynamic and Hydromagnetic Stability*, Clarendon Press, Oxford, 1961.
[7] S. M. Cox and P. C. Matthews, *Exponential time differencing for stiff systems*, Journal of Computational Physics, *176* (2002) 430–455.
[8] P. E. Dimotakis, *Turbulent mixing*, Annu. Rev. Fluid Mech., *37* (2005), 329–356.
[9] P. G. Drazin and W. H. Reid, *Hydrodynamic Stability*, Cambridge University Press, 2004.
[10] J. S. Hesthaven and T. Warburton, *Nodal Discontinuous Galerkin Methods: Algorithms, Analysis, and Applications*, Springer, 2007.
[11] T. Y. Hou and R. Li, *Removing the stiffness of variable coefficient differential equations with the Fourier method*, J. Comput. Phys., *115* (1994), 19–33.
[12] A. K. Kassam and L. N. Trefethen, *Fourth-order time-stepping for stiff PDEs*, SIAM J. Sci. Comput., *26*(4) (2005), 1214–1233.
[13] D. A. Kopriva, *Implementing Spectral Methods for Partial Differential Equations: Algorithms for Scientists and Engineers*, Springer, 2009.
[14] R. J. LeVeque, *Finite Volume Methods for Hyperbolic Problems*, Cambridge University Press, 2002.

[15] A. Miura and P. L. Pritchett, Nonlocal stability analysis of the MHD Kelvin–Helmholtz instability in a compressible plasma, *J. Geophys. Res.*, *87*(A9), (1982) 7431–7444.
[16] A. Miura, Simulation of Kelvin–Helmholtz instability in the magnetotail, *Geophys. Res. Lett.*, *11* (1984), 557–560.
[17] K. M. Owolabi, J. F. Gómez-Aguilar, Y. Karaca, Y. M. Li, B. Saley, and A. A. Aly, *Chaotic behavior in fractional Helmholtz and Kelvin-Helmholtz instability problems with Riesz operator*, Fractals, *30* (2022) 2240182.
[18] H. A. Stone, A. D. Stroock, and A. Ajdari, *Engineering flows in small devices: Microfluidics toward a lab-on-a-chip*, Annu. Rev. Fluid Mech., *36* (2004) 381–411.
[19] S. A. Thorpe, *Experiments on the instability of stratified shear flows: miscible fluids*, J. Fluid Mech., *46* (1971), 299–319.
[20] G. Tryggvason, B. Bunner, A. Esmaeeli, D. Juric, N. Al-Rawahi, W. Tauber, J. C. Han, S. Nas, and Y. J. Jan, *Direct numerical simulations of gas–liquid multiphase flows*, Computers & Fluids, *32*(2) (2003) 231–274.
[21] J. Yang, *Nonlinear Waves in Integrable and Nonintegrable Systems*, SIAM, 2010.